Chapter 4

The L3 Detector at LEP

The work described in this thesis was based on data collected by the L3 detector at the LEP e^+e^- accelerator. This chapter gives an overview of these experimental facilities, with an accent on the elements important for my physics analyses.

4.1 The LEP Collider

The Large Electron-Positron (LEP) collider [86] was designed to provide electron-positron collisions at center-of-mass energies up to about 200 GeV. It was the largest synchrotron accelerator in the world, with the main ring tunnel having a circumference of 26.67 km. The tunnel crosses the French-Swiss border near Geneva and lies between 40 and 150 m below the surface. It is composed of eight 2.9 km long arcs and eight straight sections extending 210 m on either side of the eight collision points. The four LEP experiments, L3 [87], ALEPH [88], OPAL [89], and DELPHI [90] were installed in the large experimental halls built around even-numbered collision points. The layout of the LEP ring is shown in Figure 4.1.

4.1.1 LEP Injector Chain

Before entering the LEP ring, the electrons and positrons passed through a complex system of injectors. The injector chain started with a 200 MeV electron linac. Its intense electron beam was used to produce positrons in a tungsten target. The positrons emerging from the target and electrons produced by a nearby gun were accelerated to 600 MeV by another linac. The linacs operated at 100 Hz and delivered

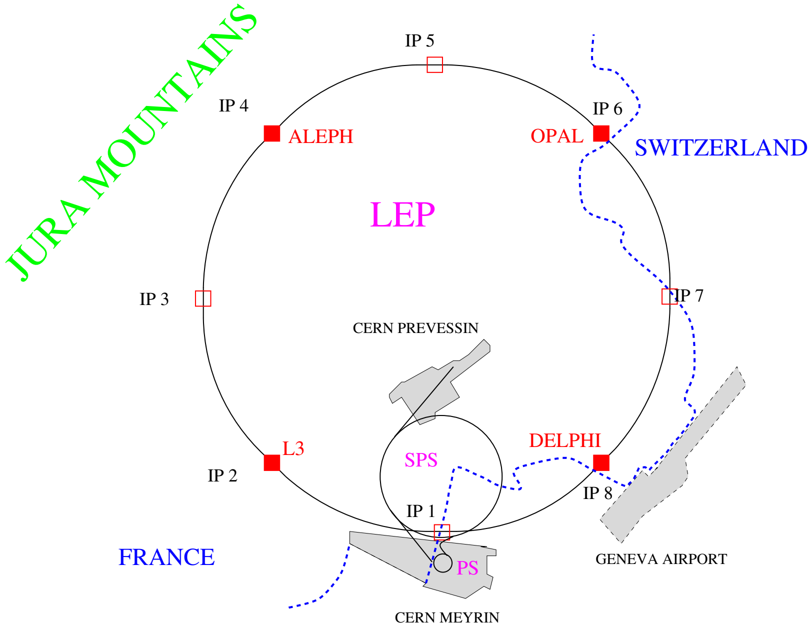

Figure 4.1: The LEP collider at CERN. The eight collision points are denoted as IP1-IP8.

the beam pulses which were then stored in eight bunches in the electron-positron accumulator ring (EPA). From the EPA, electrons and positrons were transferred to the next accelerator, the CERN Proton Synchrotron (PS), where they were accelerated to 3.5 GeV. The final element in the chain was the CERN Super Proton Synchrotron (SPS), which delivered the beams to LEP at an energy of 22 GeV. Figure 4.2 gives an overview of the LEP injector chain which is described in [91].

The advantage of building LEP at CERN was the possibility to include the already existing PS and SPS synchrotrons in the LEP injector chain. The PS is by far the oldest accelerator in use at CERN. It was built in 1959 and has a circumference of 630 m. The SPS was built in 1976 and has a circumference of 6.9 km. This accelerator allowed the breakthrough discovery of the W and Z bosons in 1983 by the UA1 and UA2 collaborations [92, 93]. Both the PS and SPS can accelerate not only electrons, but also protons and heavy ions. Moreover, the SPS was able to simultaneously operate as a LEP injector and produce stable 450 GeV proton beams for the fixed-

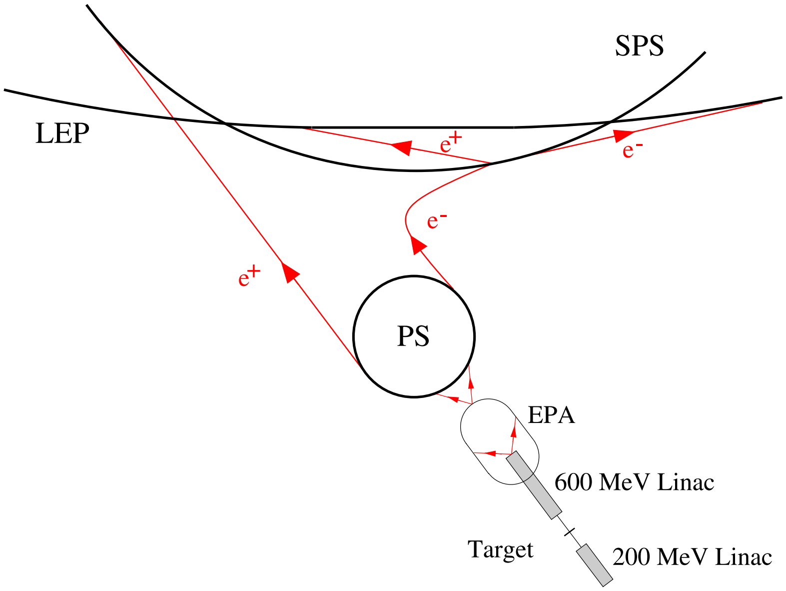

Figure 4.2: Layout of the LEP injector chain (dimensions not to scale).

target experiments. The Large Hadron Collider (LHC)[1] will soon replace LEP in its underground tunnel. However, due to their versatility, the PS and SPS synchrotrons will not be dismantled. Both of them will be used to inject proton and Pb ion beams into the LHC [94].

4.1.2 LEP Physics Program

Contrary to the fast-cycling PS and SPS, the LEP collider had a slow repetition rate. Each operation cycle, referred to as a *fill*, started by preparing the machine for injection at 22 GeV. Electrons and positrons were injected in parallel for 10-30 minutes. As soon as the filling process was finished, radio-frequency cavities accelerated the beams to the target energy at a rate of about 125 MeVs^{-1}. As electrons passed through a cell of a conducting (or superconducting) cavity, the electric fields within the cavity were timed to oscillate in the direction of acceleration. A corresponding timing was also present for the positrons, which counter-circulated in the same beam

---

[1] The LHC will be a proton-proton collider with a maximum center-of-mass energy of 14 TeV. It should either discover the Higgs Boson or disprove the existence of the Standard Model Higgs sector.

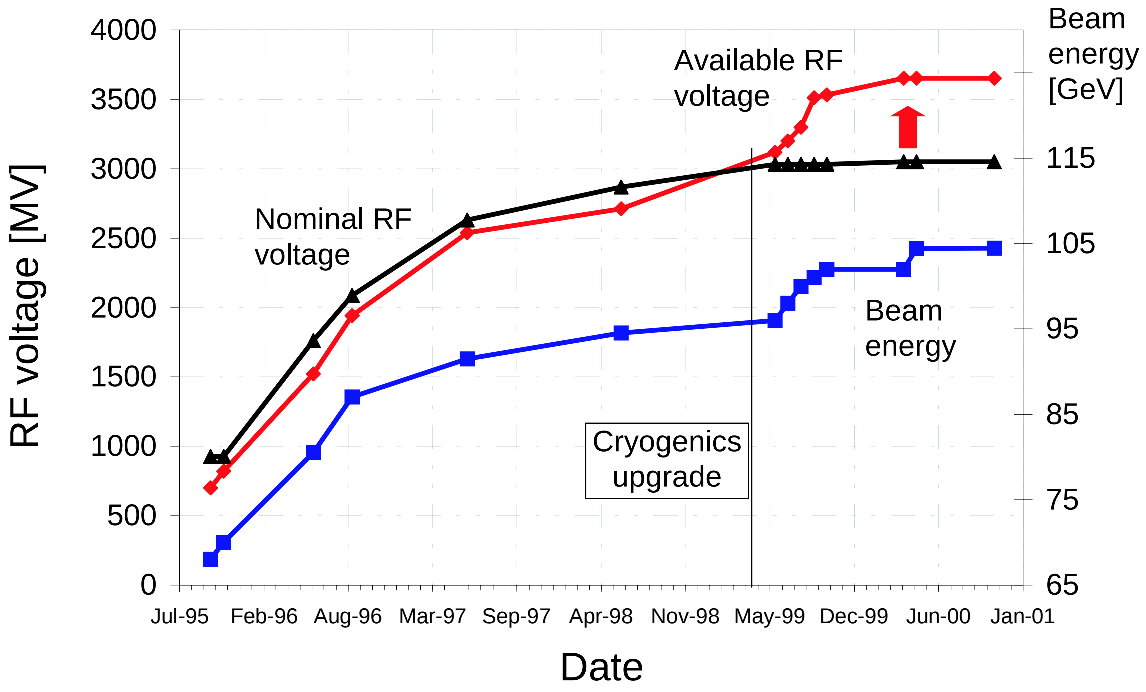

Figure 4.3: Time evolution of the LEP beam energy, the nominal (with the design accelerating gradient of 6 MV/m) and the available circumferential RF voltage.

pipe. A total of about 5400 magnets were used to focus and bend the beams into the required orbit.

LEP began operation in 1989. The LEP run from 1989 to 1995 was dedicated to precision studies of the Z boson properties. This period is referred to as LEP1. Electron-positron collisions were provided at several well-determined center-of-mass energies around the Z resonance, and the four LEP experiments collected 15.5 million Z decays into quarks plus 1.7 million leptonic Z decays. The most impressive result of the LEP1 physics program is the 2×10^{-5} accuracy on the Z boson mass measurement [95].

Starting in 1996 LEP began running at higher energies. Its center-of-mass energy gradually increased from about 90 GeV at LEP1 to almost 210 GeV in 2000, the last year of the LEP program. Attaining such high center-of-mass energies came with the high price tag of synchrotron radiation, emitted by electrons and positrons under circular acceleration in LEP. The energy loss per particle per turn due to synchrotron radiation was given by [96]

$$\Delta\mathrm{E[eV]} \simeq 8.85 \times 10^4 \, \frac{\mathrm{E^4[GeV]}}{\rho\mathrm{[m]}}\,, \tag{4.1}$$

where E was the beam energy and ρ was the average bending radius (3100 m for LEP). For a center-of-mass energy of 209 GeV, about 3.2% of the beam energy was lost per turn [97]. Thus, the maximum beam energy was limited by the available accelerating voltage provided by the RF cavities. The available accelerating voltage was increased in two ways:

- **Installation of additional RF cavities.** Between 1995 and 1999 most of the originally installed copper cavities were removed and replaced by the superconducting ones. The resulting voltage increase is shown by the graph "Nominal RF voltage" in Figure 4.3.

- **Increase of the accelerating gradient.** Until 1999, the accelerating gradient in the superconducting cavities was close to its design value of 6 MV/m [96]. After the cryogenics upgrade in 1999 it was continually improved to a maximum value of 7.5 MV/m [96] in 2000 (see Figure 4.3).

At the end of LEP its RF system consisted of 288 super-conducting cavities and 56 original copper cavities and provided more than 3.5 GV of accelerating voltage per turn.

The operation of the RF system could be disrupted by RF trips.[2] One RF trip would cause a reduction of about 100 MV in the available accelerating voltage. During the recovery time the maximum LEP beam energy was then reduced by about 0.8 GeV. The mean time between trips in 2000 was about 14 minutes, and the recovery time per trip was about 2-3 minutes. The average length of a fill at a given

---

[2] RF trips occurred on a statistical basis and were mainly produced by field emission, which could lead to local heating of cavity walls and a sharp rise in the pressure of the helium bath [97]. One trip would usually disrupt only one klystron at a time, leading to a temporary loss of eight superconducting cavities.

center-of-mass energy depended on the rate of the RF trips and the available RF margin, which was given by the difference between the maximum available RF voltage and the RF voltage required to sustain the beams at this center-of-mass energy. It was possible to operate LEP at an energy lower than the maximum one and still keep the beams during RF trips. However, at the maximum beam energy (without any RF margin) the average physics coast lasted only 14 minutes, whereas the fill set-up time was about 60 minutes. Operation at the maximum energy would be quite inefficient, and the luminosity production rate would be severely reduced. To achieve the highest effective beam energy and maintain an acceptable luminosity production level, a special ramping strategy (*mini-ramp strategy*) was implemented in the year 2000 [96]. A physics fill was started at a lower energy (2 RF trips margin), then ramped in collision to a medium energy (1 RF trip margin), and finished at the maximum beam energy (no margin). The balance between the effective energy and luminosity production rate was constantly optimized to achieve a maximum Higgs discovery potential.

The mini-ramp strategy employed in 2000 and the gradual increase of the accelerating gradient in 1999 resulted in a wide scatter of the LEP center-of-mass energies during the last two years of the LEP2 phase. Figure 4.4 shows the integrated luminosity collected by the L3 experiment during each year of the LEP2 program.[3] The data analyzed in this thesis was taken during 1998-2000, when L3 collected about 627 pb^{-1} at center-of-mass energies between 189 GeV and 208 GeV. The highest peak luminosity of about $1.2 \times 10^{32}\ \mathrm{cm}^{-2}\mathrm{s}^{-1}$ was achieved in 1999, corresponding to the average beam current of 5.5 mA (in two times 4 bunches).

LEP Beam Energy Measurement

The most important LEP operating parameter for physics studies is beam energy. At LEP1, the resonant depolarization method [98] was used to determine the beam energy to a precision of about 5 MeV [99]. The method utilized the Sokolov-Ternov effect [100] that leads to self-polarization of the beams parallel (and antiparallel) to

---

[3] The LEP2 phase officially started in 1996 when L3 collected about 20 pb^{-1} in the 160-170 GeV center-of-mass energy range.

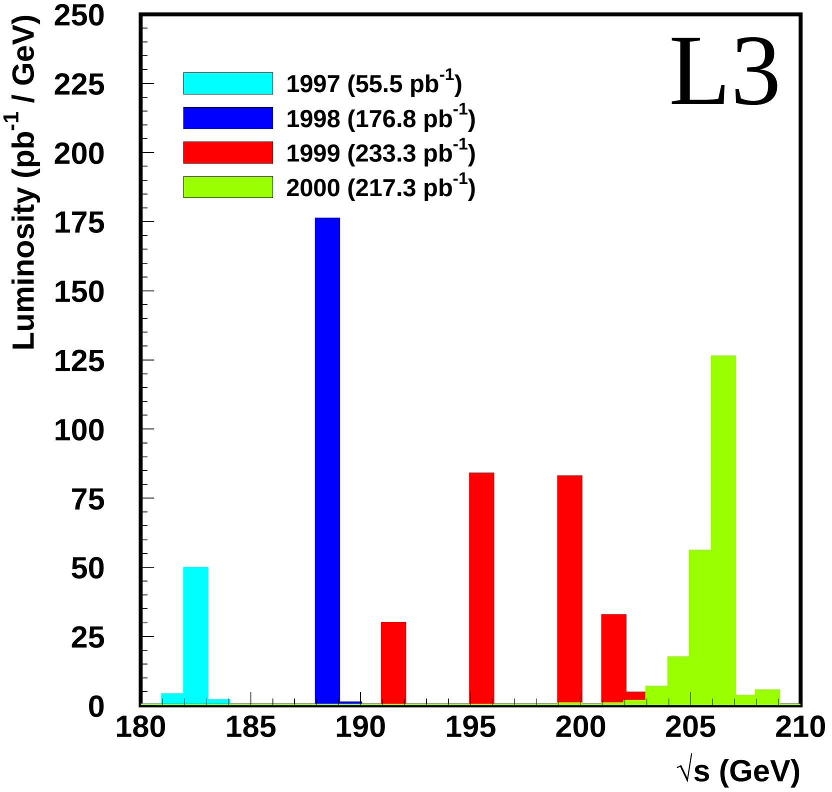

Figure 4.4: Integrated luminosity recorded by L3.

the magnetic bending field due to synchrotron radiation emission.

The precession frequency of the polarization vector was measured by inducing a resonant depolarization of the beam with a radial oscillating field from a coil. If the perturbation from the radial field was in phase with the spin precession, then the spin rotations about the direction of the perturbation field caused the spins of the particles to partially flip. About 10^4 turns or one second were needed to destroy the transverse polarization. The precession frequency was proportional to the electron's energy; thus one could extract the average beam energy by measuring the frequency of the perturbation field corresponding to the resonant depolarization.

Unfortunately, depolarizing effects due to magnetic field imperfections increased sharply with the beam energy. Thus, the method of resonant depolarization was impossible to use at beam energies above around 60 GeV. At LEP2, nuclear magnetic resonance (NMR) probes inserted in 16 of LEP dipole magnets were used to monitor the magnetic field for a relative beam energy measurement. The probes were calibrated at lower energy using the resonant depolarization method. The uncertainty of the extrapolation to the actual LEP2 beam energies proved to be the leading error on the energy measurement.

In order to check the validity of the NMR-extrapolation method and to reduce the systematic error, a special magnetic spectrometer [101] was installed in 1999. The idea was to measure the beam trajectory before and after a special dipole magnet of known integrated field, thereby directly determining the beam energy during physics running at LEP2. Good agreement between the magnetic spectrometer and NMR-extrapolation methods was observed [102], and the total error on the LEP beam energy was estimated [103] to be about 11 MeV (or $\simeq$0.01%) and 20 MeV (0.02%) for the data taken in 1998-1999 and in 2000, respectively.[4]

4.2 The L3 Detector

The L3 detector was designed to reconstruct and identify particles produced in e^+e^- interactions and provide accurate measurements of both particle momenta and energies. Compared to the other three detectors at LEP, L3 emphasized precise energy measurements of electrons, photons, and muons. The majority of the detectors installed at particle colliders, including the L3 detector, may be described as a series of cylindrical, concentric subdetectors arranged around the beam pipe with the interaction point at the center and a set of endcap subdetectors covering the ends of the cylinders. The layout of the L3 detector is depicted in Figure 4.5.

Particles produced at the interaction point and traveling outwards through the L3 detector first encountered a set of two tracking subdetectors designed primarily to give information on the trajectories of charged particles (tracks). Since a surrounding coil provided a strong magnetic field inside the entire detector, the curvature of the track yielded the particle momentum. The particles then reached a high-density calorimeter

---

[4] The significant increase in uncertainty for 2000 was associated with a special magnetic field configuration, which was used in that year in order to boost the beam energy.

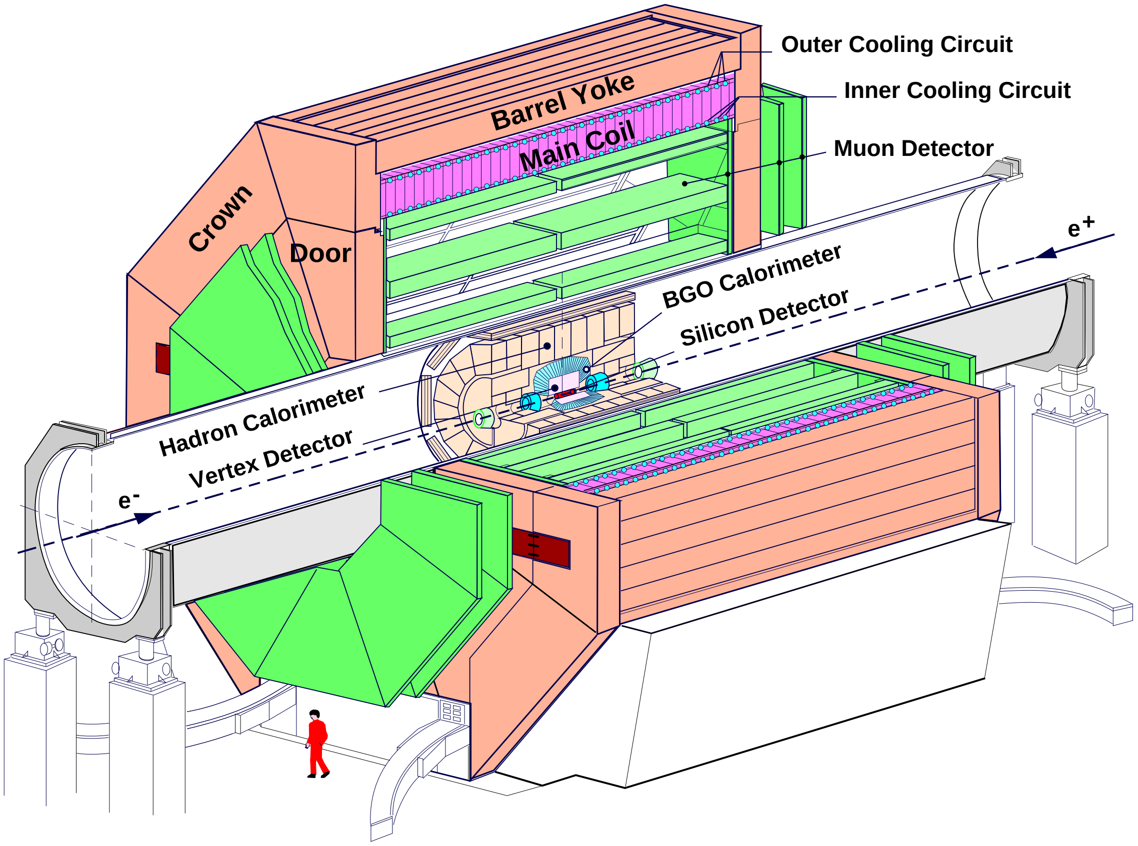

Figure 4.5: Perspective cut-away view of the L3 detector, showing the location of the subdetectors, the support tube and the magnet.

arrangement designed to help identify them and/or evaluate their energies. Any particles that managed to pass through the calorimeters entered the muon chambers designed to tag (identify) muons and measure their momenta. The tracking system and calorimeters were contained in a steel tube, which also supported the muon chambers and maintained the alignment of the subdetectors. Figure 4.6 shows a side view of the inner L3 detector.

The Cartesian (x,y,z) coordinate system used within L3 has its origin at the interaction point, which is also the geometrical center of the detector. The z-axis runs parallel to the beam-pipe in the electron beam direction. The x-axis points towards the center of LEP, while the y-axis points vertically upwards. A cylindrical coordinate system is also used with the origin and z-axis coinciding with those of the Cartesian

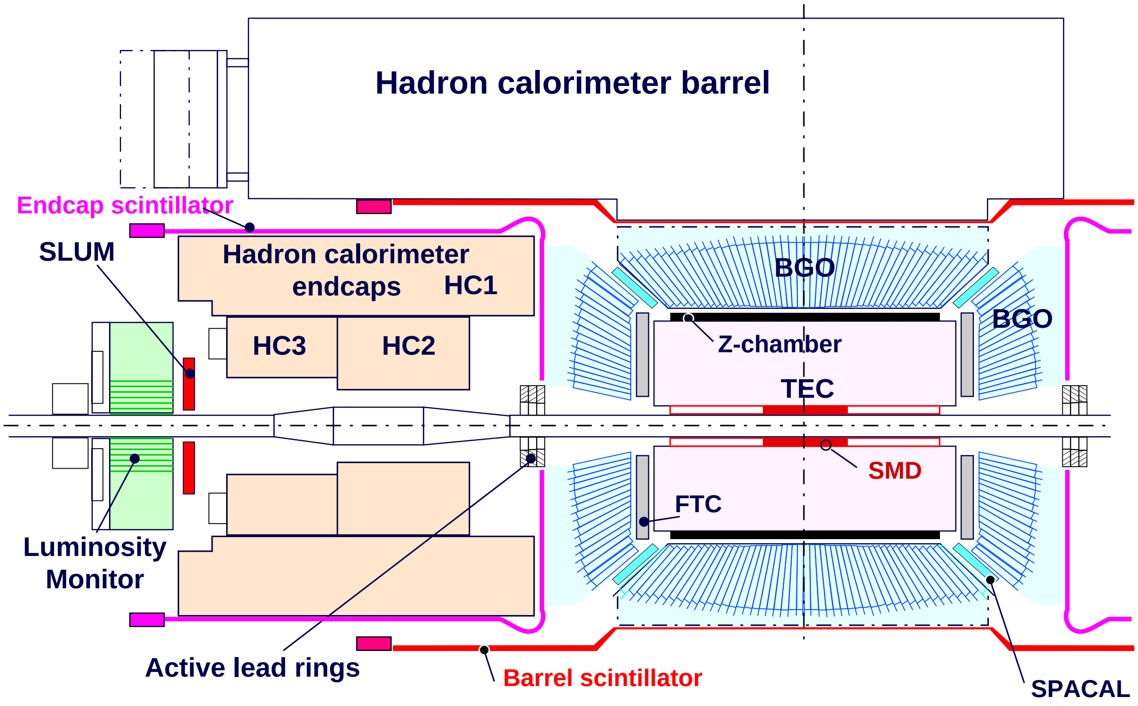

Figure 4.6: A schematic representation of the inner components of the L3 detector. In addition to the tracking system (TEC, SMD, and FTC) and the calorimeters, also shown are the active lead rings, the luminosity monitor, and the scintillators.

system. The planes $\phi = 0^\circ$ and $\phi = 90^\circ$ contain the x-axis and y-axis, respectively, with $r = \sqrt{x^2 + y^2}$. In addition, it is often useful to refer to the polar angle θ with respect to the z-axis.

A detailed description of the L3 detector is given in [87]. It should be noted that L3 had been undergoing constant modification[5] during the LEP1 and the beginning of the LEP2 phase. This analysis, however, is only concerned with the data-taking period of 1998-2000, when the detector configuration remained unchanged. The most important subdetector for the analysis presented in this thesis was the electromagnetic calorimeter since it provided a precise measurement of photon energies and flight directions. Nevertheless, all other L3 subdetectors were relevant to the selection of the single- and multi-photon events. They were used to reject background events

---

[5] Only the original components of the L3 detector are covered in [87]. References to papers describing the detector upgrades will be given when needed.

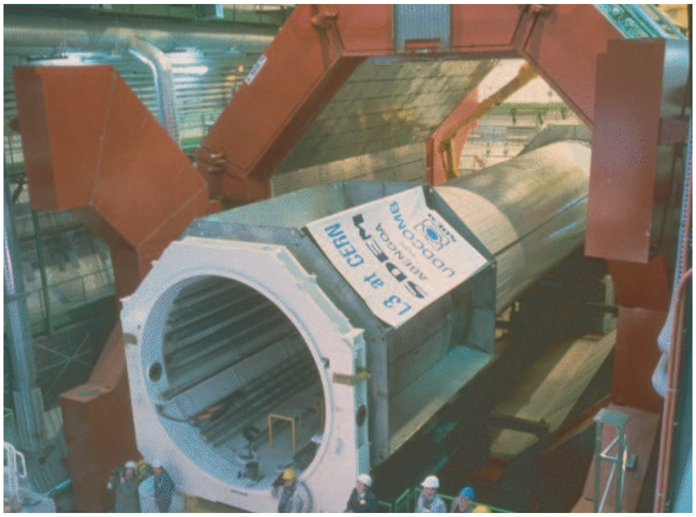

Figure 4.7: The Magnet and Support Tube during their installation at L3. The doors of the magnet are open and the support tube has been positioned along the center of the magnet.

from other Standard Model processes and from cosmic rays. The description of the L3 subdetectors follows.

4.2.1 The Magnet

A large magnet with a relatively low field was chosen in order to optimize the muon momentum resolution, which improved linearly with the field but quadratically with the lever arm. The magnet is composed of a water-cooled solenoid coil, a soft iron yoke, and two steel endcaps that provide support for the yoke. The magnet has an outside radius of 7.9 m, an inside radius of 5.9 m, and is 11.9 m in length. The total weight of the L3 magnet is 7800 tons.[6]

The magnet (see Figure 4.7) surrounded the entire L3 detector[7] providing a 0.5 T field parallel to the beam axis. The magnetic field was mapped inside the support tube with Hall probes and outside with about 1000 magnetoresistors and 5 NMR probes.

---

[6] The L3 magnet was included in the 1997 Guinness Book of Records as the World's Largest Electromagnet.

[7] Except for a part of the forward-backward muon spectrometer.

It is interesting to note that the L3 magnet is the only part of the L3 detector which will be used for the LHC program. The ALICE experiment [104] is currently being built inside the L3 magnet to study lead-ion as well as proton-proton collisions at the LHC.

4.2.2 Central Tracking Detectors

The central tracking system was used to identify charged particles and to measure their trajectories (tracks). It included a Time Expansion Chamber (TEC) and a Silicon Microvertex Detector (SMD). Additional measurements of the z-coordinate were obtained from the Z-chamber and the Forward Tracking Chambers (FTC) (Figure 4.6). Due to the limited space available inside the electromagnetic calorimeter, the TEC had only a modest lever arm of 31.7 cm, and as pointed out previously, the L3 magnetic field was relatively weak.

The design goal of TEC was to identify the charge of 50 GeV particles at 95% confidence level. That target was met by choosing a drift chamber design in which a relatively large low-field drift region was separated from a high-field amplification region by two planes of grounded wires. Charged particles traversing the gas volume of TEC caused ionization of the gas atoms. The ionization electrons would then drift to the anode wires (Figure 4.8), and the drift times of these electrons could be used to reconstruct the track position. The drift times were precisely determined by measuring the centroids of the arrival time distributions collected by each anode wire. A drift velocity of about 6 μm/ns was attained in the low-field region, whereas in the amplification region it was about 50 μm/ns [105]. The drift velocity was precisely determined *in situ* using a gas test chamber and was kept constant within 0.1% [106].

The TEC was composed of two concentric cylindrical drift chambers, divided into 12 inner and 24 outer sectors. Each sector had a central anode plane and was separated from its neighbouring sectors by cathode planes. The TEC wires were arranged parallel to the z-axis so that the coordinate measurement was made in the bending plane. The inner (outer) sectors contained 8 (54) anode wires each.

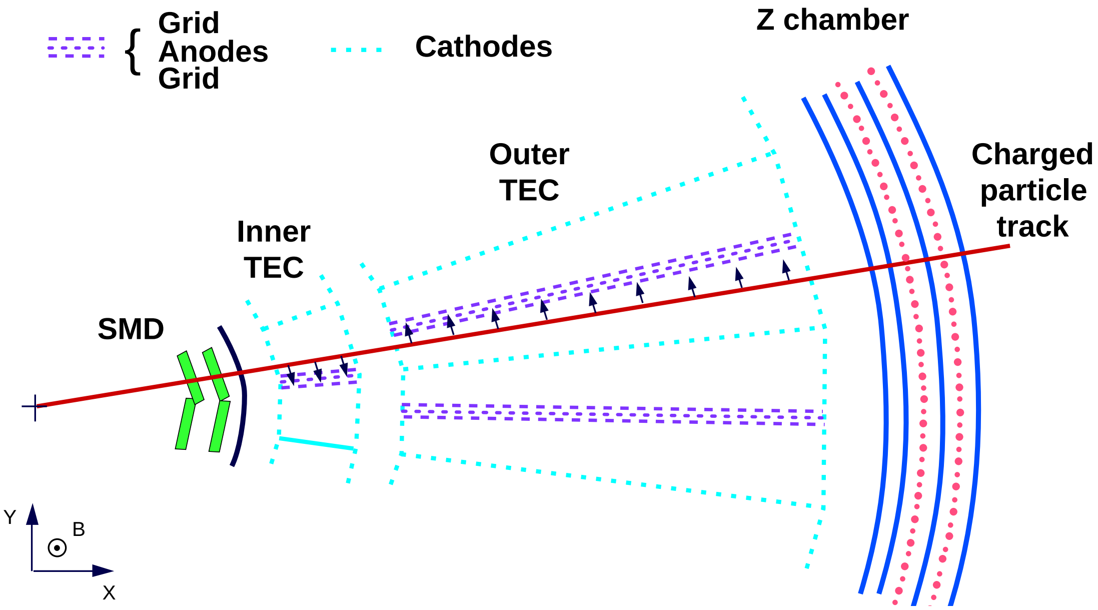

Figure 4.8: A charged particle produced within the beam pipe would first cross the SMD, then the TEC, and finally the Z-Chamber before hitting the calorimetry. The geometry of a TEC sector is shown in detail.

A detailed $r\phi$ view of the L3 tracking system is shown in Figure 4.8. The sensitive region in which the traversing tracks could be measured by all 62 anode wires was $44^\circ < \theta < 136^\circ$. Particles with $\theta(180^\circ - \theta) < 10^\circ$ could not be detected by the TEC.

The expansion of the drift time provided detectable time differences between hits from neighbouring tracks. Typically hits separated by 500 μm were reconstructed individually. The excellent double track resolution proved to be useful in the selection of converted photons. This will be discussed in more detail in Chapter 6, Section 6.3.4.

The z-coordinate of a track was measured by the Z-chamber, which consisted of two proportional wire chambers surrounding the cylindrical outer surface of TEC. It was read out by cathode strips tilted with respect to the z-axis and covering the angular region of $45^\circ < \theta < 135^\circ$. The spatial resolution of the Z-chamber was about 300 μm. In the forward region the FTC was used to measure the x-y coordinates of a track at fixed z. These proportional chambers were located between the TEC and electromagnetic calorimeter endcaps and covered polar angles $12^\circ < \theta(180^\circ - \theta) < 34^\circ$.

The SMD [107] consisted of two radial layers of double-sided silicon strip detectors located at distances of 6 cm and 8 cm from the beam axis and covering polar angles $22^\circ < \theta < 158^\circ$. It provided ϕ and z measurements with approximately 10 μm accuracy. The SMD significantly improved the momentum and vertex resolution of the tracking system by providing two additional points close to the interaction point for each reconstructed track.

The combined TEC-SMD transverse momentum resolution at large polar angles ($\theta > 45^\circ$) was $\sigma(1/P_T) = 0.015\ \mathrm{GeV}^{-1}$. The angular resolution was found to be $\sigma_\phi = 0.6$ mrad and $\sigma_\theta = 3.4$ mrad.

4.2.3 Electromagnetic Calorimeter

The physics analysis that I present in this thesis relied heavily on the electromagnetic calorimeter (ECAL) of the L3 detector. In this section I describe the construction principle, the geometry, and the readout chain of the ECAL. This discussion will be continued in the next chapter, where I will describe its particle reconstruction algorithm as well as its calibration and monitoring.

The L3 ECAL was designed to provide excellent energy and spatial resolution for photons and electrons over a wide energy range, from 100 MeV to 100 GeV. As I will discuss in Section 5.6, it was precisely calibrated using an RFQ accelerator and its energy resolution was measured to be: $\sigma(E)/E = 3.2\,\%/\sqrt{E} \oplus 0.9\,\%$ (E in GeV). The L3 ECAL was a total absorption calorimeter made of 10,734 bismuth germanium oxide (BGO) crystals. The crystals pointed directly towards the L3 interaction point and were arranged to form two symmetrical half-barrels surrounding the TEC and two endcaps mounted behind the FTC. The geometry of the BGO calorimeter is illustrated in Figure 4.9.

Electromagnetic Showers in the BGO Crystals

At energies above 100 MeV, electrons and positrons traversing dense matter lose their energy primarily through the bremsstrahlung process [6], radiating photons as a result

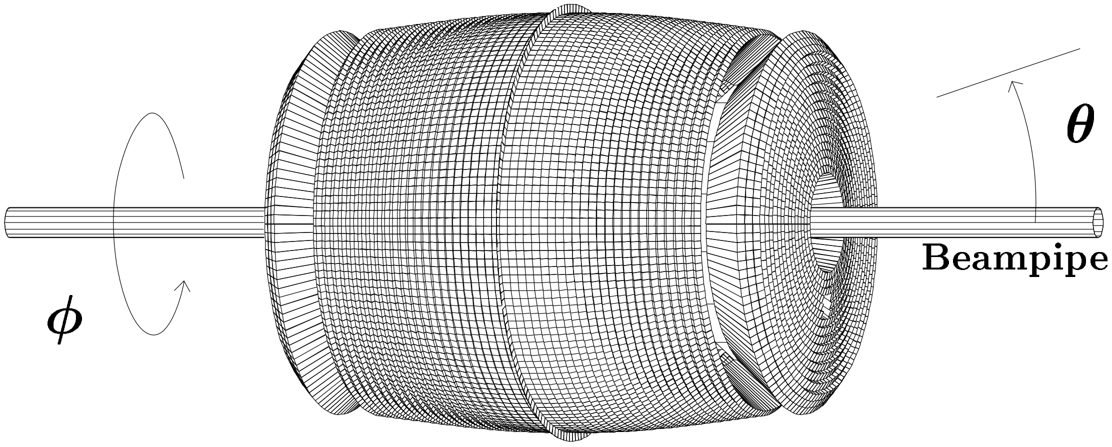

Figure 4.9: The BGO electromagnetic calorimeter.

of the Coulomb interaction with the electric fields of the atomic nuclei:

$$\mathrm{e}^{\pm}(N) \rightarrow \mathrm{e}^{\pm} + \gamma\,,$$

where (N) represents the interaction with the Coulomb field of the nucleus. Similarly, photons with energies greater than 10 MeV interact with the matter predominantly through the process of electron-positron pair production:

$$\gamma(N) \rightarrow \mathrm{e}^{+} + \mathrm{e}^{-}.$$

Both pair production and bremsstrahlung processes produce secondary photons and electrons which can also interact with the material. The resulting chain reaction is called an *electromagnetic shower* [6]. As the shower develops, the energy of its constituents decreases and other energy loss processes start to contribute. Eventually, the energy of all particles produced in the shower is absorbed by the showering material. Since high-energy photons and electrons generate the same chain reactions originating from different initial interactions, they produce showers that are virtually indistinguishable.[8] The physics of electromagnetic showers and calorimeters is described in detail in [108].

---

[8] Contrary to electrons, high energy photons traveled, on average, 1.5 cm before converting into an $\mathrm{e}^{+} + \mathrm{e}^{-}$ pair [108]. However, this difference in the shower maximum position could not be detected since the BGO calorimeter had no longitudinal segmentation.

To describe the shower development in a material-independent way, units of *radiation length* and *Molière radius* are frequently used. The numerical values of these two units depend only on the showering material. The radiation length (X_0) is defined as a distance over which a high energy (E > 1 GeV) electron loses approximately 63% (i.e., $1 - \mathrm{e}^{-1}$) of its energy. The Molière radius (R_M) describes the lateral shower profile, where approximately 90% of the shower is typically contained in a cylinder of radius R_M around the shower axis. The BGO inorganic crystal scintillator was chosen to be used in L3 because of its very short radiation length and Molière radius, $X_0 = 1.12$ cm and $R_M = 2.4$ cm, and because of its high scintillation light yield. The high stopping power of the BGO translated into the compactness of the calorimeter, which was important due to limited space available inside the support tube.

In a BGO crystal, the passage of low-energy electrons and positrons ($\mathrm{E} \leq 10$ MeV) through the crystal lattice causes short-lived excitations in the system of lattice electrons. The decay of lattice excitations produces scintillation photons with a wavelength spectrum peaked at about 480 nm (green light). The amount of the scintillation light is proportional to the deposited energy ($\simeq 2.8 \times 10^3\,\gamma/\mathrm{MeV}$). Since the BGO crystals are optically transparent, the scintillation light can be detected and used to compute the energy of the electromagnetic shower.

The Geometry of the Electromagnetic Calorimeter

The BGO crystals of the L3 electromagnetic calorimeter had a truncated pyramidal shape (Figure 4.10) with a front surface of $\simeq 2 \times 2\,cm^2$, a rear surface of $\simeq 3 \times 3\,cm^2$, and a depth of about 21.5 radiation lengths (24 cm). To minimize the mechanical stress, each crystal was housed in its own cell of a carbon fiber support structure. The walls between the crystals were about 0.2 mm thick. The dead material of the walls together with the clearances represented about 2.1% of the solid angle coverage of the ECAL.

The crystals were aligned with their axes pointing to the interaction point, but with a slight tilt to reduce the number of particles escaping detection in the gaps between the crystals.

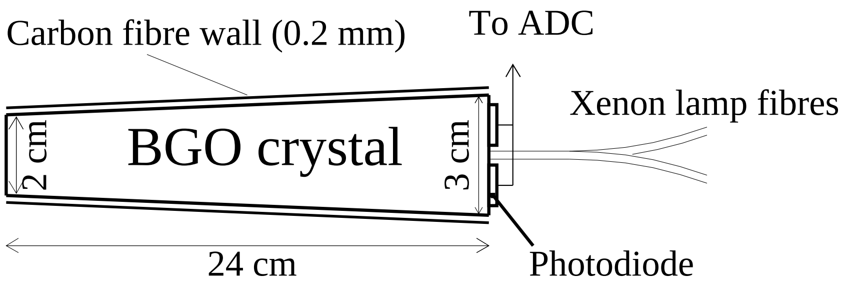

Figure 4.10: A BGO crystal.

The BGO calorimeter consisted of the following four large crystal arrays.

- **Two half-barrels.** Each half-barrel contained 3840 crystals that were arranged in a 160 × 24 matrix in the $\phi - \theta$ plane. The combined total angular coverage of the BGO barrel was $42.3° < \theta < 137.7°$. The 160 ϕ-slices of 24 crystals were tilted by about 0.6° to aim at a position 5 mm away from the interaction point.

- **Two endcaps.** Each endcap was made of 1527 crystals arranged into six large rings. Each of the large rings was made of three crystals in θ-coordinate (three individual θ − rings), except for the inner one which contained only two θ − rings. The number of crystals in ϕ varied from 48 in the inner ring to 128 in the outer ring.[9] Nine crystals were taken out from each endcap at $\phi \simeq 270°$ and $\theta(180° - \theta) \simeq 16°$ to create a hole for the beam pipe of the RFQ calibration system, which will be described in Chapter 5. The endcaps were installed in 1991. Unfortunately, the construction of the central tracking system required more space than was originally foreseen. Therefore the endcaps had to be displaced by a distance of about ±13 cm along the z-axis and covered $9.9° < \theta(180° - \theta) < 36.8°$. This configuration induced a θ-tilt of $2.1° - 5.4°$ with respect to the nominal direction to the interaction point. The tilt in ϕ was 0.6°, the same as for the crystals in the barrel.

---

[9] The exact numerical values for the six large rings were 48, 64, 80, 96, 112, and 128.

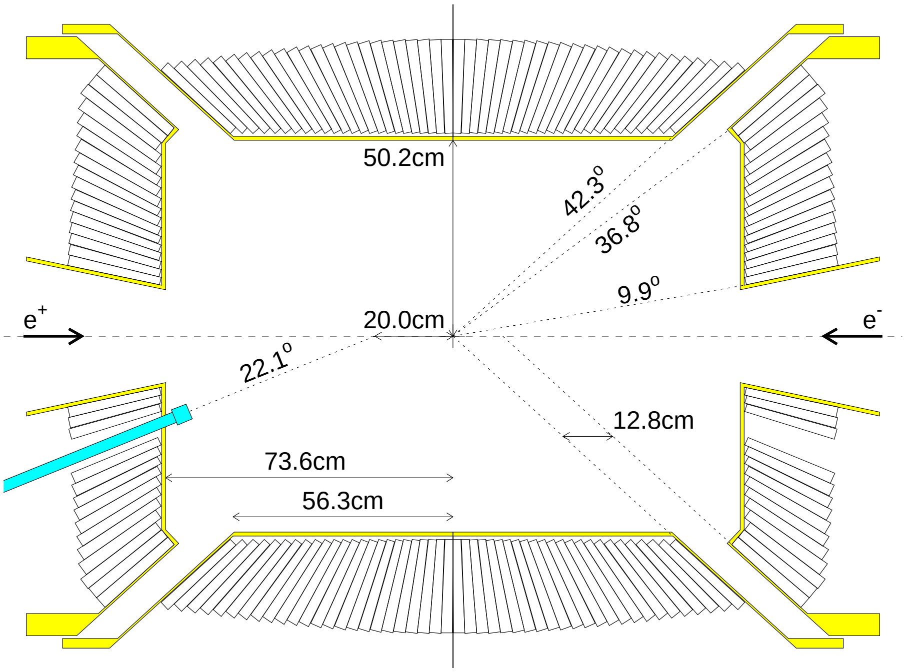

Figure 4.11: A side view of the L3 electromagnetic calorimeter in the vertical $y - z$ plane. The beam pipe in the bottom left corner is part of the RFQ calibration system developed by the Caltech L3 group.

Figure 4.11 shows a cross section of the BGO calorimeter in the vertical $y - z$ plane. The dimensions of the calorimeter are also shown. Due to the angular interval between the barrel and the endcaps, the solid angle coverage of the BGO was about 92.1% of 4π steradians.

The BGO Readout System

Achieving good linearity and energy resolution required a nearly uniform light collection efficiency. The light flux collected at the rear face of a polished BGO crystal decreased strongly (up to 50%) with the distance from the front face. After coating the crystals with a 40-50 μm thick layer of high reflectivity white paint, the maximum variations in the collected light flux as a function of the distance from the front face were only about 5%.[10]

---

[10] The variations in the crystal light yield were measured using cosmic muons and were required to be less than 10% for all accepted BGO crystals [109].

To detect the BGO scintillation light a pair of silicon photodiodes were glued to a rear surface of each crystal (Figure 4.10). There were two reasons to choose photodiodes over conventional photomultiplier tubes: 1) photodiodes were not sensitive to the L3 magnetic field; 2) they took very little space. The photodiodes had a sensitive area of 1.5 cm^2 each and were read out as a single unit. Their quantum efficiency was about 70% at 480 nm, resulting in a charge deposition of about 0.2 fC (1200 electrons) per MeV of the shower energy. After preamplification and shaping, the signal from each individual crystal was split into three separate signals which were then processed by the first-level trigger and by two independent pulse-height analyses optimized for small (*low energy chain*) and large (*high energy chain*) signal amplitudes. The low energy chain was amplified by a factor of 32 with respect to the high energy chain, after which the two chains were processed identically.

The signal in each chain was first integrated and then stored in a sample and hold circuit. The stored signal was further amplified in two stages, each with a gain of four, resulting in a total of six levels of amplification for the two chains. A specifically designed analog to digital converter (ADC) was then used to digitize the collected signal of each crystal. The *floating-point* design of the BGO ADCs utilized an accurate 12-bit ADC with a 220 μs conversion time to cover 21 bits of effective dynamic range with six different amplifications[11] [110].

The first step of the digitization was to choose the level of amplification (or gain) that provided the largest unsaturated signal. When the input signal for a particular amplification approached the maximum voltage of the 12-bit ADC, the next lower amplification was used for the digitization. This design resulted in a 12-bit digitization, which together with the 9-bit (1:512) selectable gain corresponded to the effective 21-bit dynamic range. A digitization accuracy of at least 0.1% was achieved for the BGO signals above 100 MeV. The actual dynamic range extended from about 1 MeV up to 200 GeV. The energy equivalent of the transition between different gains depended on gain calibrations, pedestals, and energy calibrations. The distribution of the transition energies is plotted in Figure 4.12.

---

[11] The six signal amplifications corresponded to approximately 1, 2^2, 2^4, 2^5, 2^7, and 2^9.

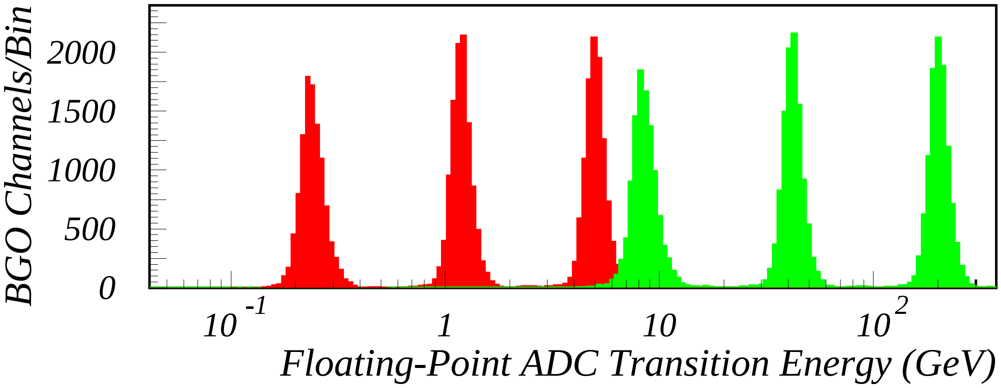

Figure 4.12: The distribution of transition energies of all BGO ADCs. The three peaks on the left correspond to the low energy channel, the peaks on the right correspond to the high energy channel.

Performance of the BGO Calorimeter

High intrinsic resolution, precise calibration, and a relatively low amount of material between the crystals and the interaction point were the main factors that made the BGO[12] the best electromagnetic calorimeter at LEP2. Its energy resolution, $\sigma(E)/E$, was better than 2% for electrons and photons with energies above 5 GeV. The linearity of the BGO response in the energy range of 1-100 GeV proved to be better than 1%.

To compare the electromagnetic calorimeters of the four LEP experiments, it is convenient to compare their measured energy resolutions for 45 GeV electrons and positrons.[13] The energy resolution of the L3 BGO for such electrons was approximately 1.0%, whereas the resolutions of the ALEPH, OPAL, and DELPHI (HPC) calorimeters were about 3.5% [111], 4.0% [112], and 6.5% [113], respectively.

The energy reconstruction algorithm of the BGO, its calibration and monitoring, as well as its performance will be described in detail in Chapter 5.

---

[12] In L3 the BGO electromagnetic calorimeter is most often referred to as simply the BGO.

[13] The reasoning behind the choice of the 45 GeV electrons will be explained in Chapter 5, Section 5.6.2. In addition, 45 GeV corresponds to approximately the middle point of the energy range 1-100 GeV, the region of interest for the analysis described in this thesis.

Gap Filler

In 1996, the gaps between the BGO barrel and the endcaps were equipped with *ECAL GAP filler* (EGAP) [114]. The EGAP counters consisted of 48 bricks of lead with a set of scintillating fibers embedded inside each brick. Its energy resolution for 45 GeV electrons was expected to be about 4.0%, significantly worse than that of the BGO. In 1998, a dedicated study of the EGAP performance *in situ* was carried out using Bhabha scattering events, $e^+e^- \to e^+e^-$. The selected events were required to have two back-to-back TEC tracks pointing in the direction of EGAP. The study showed that about 10% of such electrons passed undetected, much more than was expected from an early simulation of the EGAP response [115]. Because of this large detection inefficiency, I did not use the EGAP to identify and measure photons.[14]

4.2.4 Scintillation Counters

The L3 scintillation counter system [116] was composed of 30 barrel counters and 2×16 endcap counters. As shown in Figure 4.6, the counters were located between the BGO and hadron calorimeters and covered polar angles of $11.5^\circ < \theta < 168.5^\circ$. The scintillators were designed for a precision measurement of the relative timing of charged particles traversing the detector. The timing resolution was about 0.8 ns in the barrel and 1.9 ns in the endcaps. The scintillation counters were indispensable for the rejection of the background from out-of-time cosmic rays.

4.2.5 Hadron Calorimeter

Hadronic showers develop in a similar manner to electromagnetic ones, but are more complex as they involve both the electromagnetic and the strong interactions. The shower dimensions are governed by the nuclear interaction length of the absorber medium, which is defined as an average distance a high-energy hadron has to travel inside that medium before a nuclear interaction occurs [108]. The BGO calorimeter

---

[14] The EGAP was never used in any of the L3 analyses requiring precise measurement of photons or electrons.

corresponded to only about one nuclear interaction length and, obviously, could not be used to stop and measure hadrons. The hadron calorimeter (HCAL) was built for this purpose.

The HCAL surrounded the BGO calorimeter and was made of depleted uranium and brass absorber plates interleaved with proportional wire chambers. Its barrel covered the central region $35^\circ < \theta < 145^\circ$, while the endcaps covered $5.5^\circ < \theta(180^\circ - \theta) < 35^\circ$. The hadron calorimeter covered approximately 99.5% of the full solid angle of 4π steradians. The L3 HCAL is depicted in Figure 4.13.

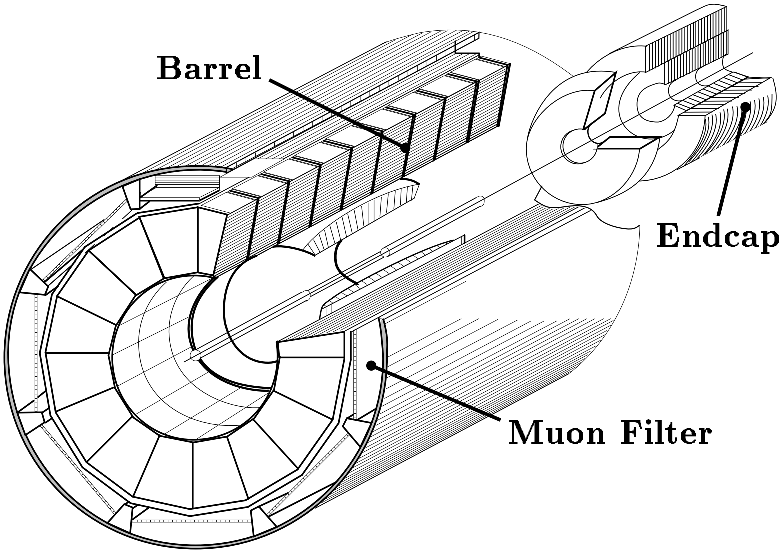

Figure 4.13: A perspective view of the hadron calorimeter and the muon filter.

The barrel had a modular structure consisting of 9 rings in θ of 16 modules in ϕ each. Each module was composed of radially stacked alternating layers of 5 mm thick depleted uranium absorber and 5.6 mm thick brass wire chambers. The modules in the middle three rings contained 58 layers of chambers each, while the modules in the other six rings contained 53 layers. Successive chambers were aligned with wires perpendicular to each other. The wires were then grouped into towers with the following readout segmentation: $\Delta\phi \simeq 2.5^\circ$, $\Delta z \simeq 6cm$, and $\Delta r \simeq 8cm$. The total number of readout channels was 23,040. Viewed from the interaction point, the HCAL barrel represented 3.5-5.5 nuclear interaction lengths. The high granularity of the barrel was successfully used in my search for long-lived neutralinos (see Chapter 7). Prior to their installation in L3, the HCAL modules were tested in test beams. The measured energy resolution for hadrons was found to be: $\sigma(E)/E = (55/\sqrt{E} + 5)\%$ [87].

The HCAL endcaps were each divided into 6 modules making up 3 rings. Viewed from the interaction point, the endcaps represented 6-7 nuclear interaction lengths.

Muon Filter

The muon filter was designed to ensure that hadronic showers were contained inside the support tube. In addition, the muon filter protected the muon chambers from the uranium noise of HCAL. The muon filter was mounted on the inside wall of the support tube and provided another nuclear interaction length behind the HCAL barrel. It was divided into eight identical octants (Figure 4.13), each made of six layers of 10 mm thick brass absorber plates, interleaved with five layers of proportional chambers, and followed by five 15 mm thick absorber plates matching the circular shape of the support tube. The material of the support tube contributed an additional 0.5 nuclear interaction lengths.

Each octant was 4 m long, 1.4 m wide and contained 78 proportional chambers. The proportional chambers were aligned parallel to the z-axis. The segment of the muon track passing through an octant was determined with a precision better than 1.5 mm in the $r\phi$ plane [117]. The overall chamber efficiency measured using test beams was about 97% [87]. The muon filter was used in my search for long-lived neutralinos to reject the background from cosmic rays, as discussed in Chapter 7.

4.2.6 Muon Spectrometer

The barrel muon chamber system (MUCH) consisted of three layers of drift chambers arranged in eight octants. The MUCH was located between the support tube and the magnet, as shown Figure 4.5, and covered the angular range $43° < \theta < 137°$. Each octant contained three layers of *P-chambers* measuring the $r\phi$ coordinates and two

Z-chambers (located in the inner and outer layers) measuring the z-coordinate of the muon track. The momentum resolution $\sigma(P_T)/P_T$ for 45 GeV muons was found to be about 4.0% [118].

The forward-backward muon chambers (endcaps) extended the angular coverage of the muon spectrometer down to $\theta > 22^\circ$ with respect to the beam axis. Both endcaps consisted of three layers of drift chambers mounted on the 90 cm thick magnet doors, and the momentum resolution of the endcaps was limited by multiple scattering in the magnet doors. Depending on the muon polar angle, it varied from 12% to 32% for 45 GeV muons [118].

The muon spectrometer was used in my single-photon selection to identify and reject cosmic ray events.

4.2.7 Active Lead Rings

The *Active Lead Rings* detector (ALR) played an important role in the analysis presented in this thesis. I used the ALR to tag radiative Bhabha scattering events, $e^+e^- \rightarrow e^+e^-\gamma$. Not only was this reaction the dominant source of background, but the selected sample of radiative Bhabha events was also used for several important detector checks as will be discussed in Chapter 6.

The ALR [119] was composed of two identical detectors covering polar angles $3.9^\circ < \theta(180^\circ - \theta) < 8.7^\circ$. The detectors were situated between the BGO and the HCAL about one meter away from the interaction point in $+z$ and $-z$ directions (see Figure 4.6). Originally installed to protect the inner tracker from beam-related background, the ALR was upgraded in 1995 to improve its resolution and reliability. Each detector consisted of seven 18.5 mm thick lead rings interleaved with five scintillator rings which were segmented in θ and ϕ. Figure 4.14 shows the structure of the ALR and the segmentation of the scintillator layers. An energy resolution of 15% was obtained for a selected sample of 45 GeV Bhabha electrons. The same Bhabha sample was used to check the angular resolutions. They were measured to be 0.2° in θ and 2° in ϕ [120].

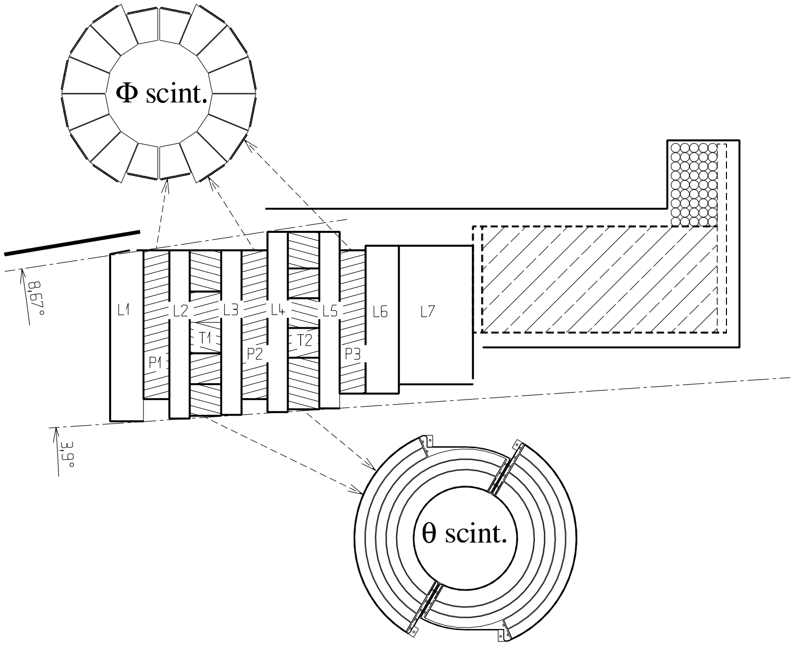

Figure 4.14: A side view of one of the two L3 ALR detectors. The segmentation scheme of the scintillator layers is also shown. The interaction point is located about one meter to the left (not shown on the plot).

4.2.8 Luminosity Monitors

The majority of the Standard Model measurements and searches for new physics at L3 require an accurate knowledge of the LEP luminosity. Bhabha scattering at low polar angles is generally used as a tool to measure luminosity at e^+e^- colliders. The differential cross section ($d\sigma/d\Omega$) of this process can be calculated theoretically to a very high precision ($\simeq$ 0.1%) [121] and grows as $1/\theta^4$. Using a sample of $N_{e^+e^-}$ selected Bhabha events, the luminosity can be derived from

$$\mathcal{L} = \frac{N_{e^+e^-}}{\sigma_{e^+e^-}\varepsilon}, \tag{4.2}$$

where ε is the selection efficiency and $\sigma_{e^+e^-}$ is the accepted cross section.

The L3 luminosity detector [122] consisted of a BGO calorimeter (LUMI) and a silicon tracker (SLUM), installed in front of the LUMI. As shown in Figure 4.6, the detectors were installed at a distance of 2.7 m from the interaction point, covering

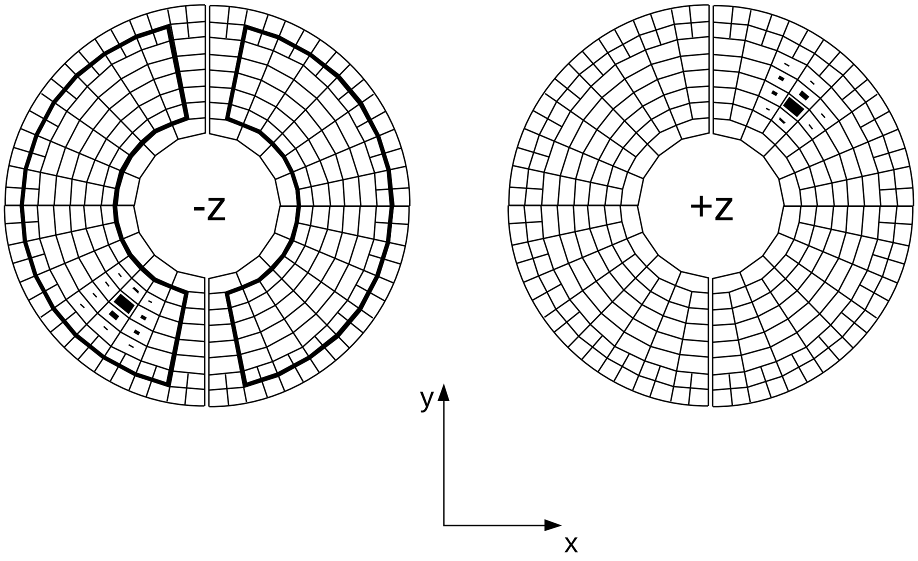

Figure 4.15: A Bhabha event observed in the LUMI. The sizes of the black areas are proportional to the energy deposited in each crystal. The contour on the left-hand side indicates the fiducial volume used for the luminosity measurement.

the angular range $1.4^\circ < \theta(180^\circ - \theta) < 3.9^\circ$. Each of the two LUMI calorimeters contained 304 BGO crystals (see Figure 4.15) and had an energy resolution of 2%. The SLUM was installed in 1993 to improve the angular resolution of the system.

The precision of the luminosity measurement by L3 was dominated by systematic uncertainties and was about 0.2% for the data sets I used.

4.2.9 L3 Trigger System

The LEP beam crossing frequency was about 45 kHz, while the L3 data acquisition system could not cope with rates in excess of about 10 Hz. The L3 trigger system [123] was designed to act as a filter that would decide whether an "interesting" e^+e^- event took place. This system rejected background processes (e.g., beam gas or cosmic ray events) and detector noise signals while maintaining a high efficiency for recording interesting physics processes.

Triggering at L3 was performed in three steps (levels) of increasing complexity.

The level 1 trigger consisted of five independent triggers which used signals from different L3 subdetectors. In case of a positive decision the detector data was digitized and stored within 500 μs in multi-event buffers. During that time interval the L3 readout system would not accept any new input and all further data taking would be blocked ("dead time"). The "dead time" at LEP2 was typically about 7% [124]. Negative trigger decisions did not affect the L3 readout chain since the electronics were cleared before the next beam crossing. The level 1 trigger accepted events at a rate of 15-20 Hz. Events with a coincidence of at least two level 1 triggers were automatically accepted by L3 and were written on tape.

The level 2 trigger worked in parallel with the level one trigger and used the same information. However, as it had more time available, it could use more complex algorithms. It accepted events on the basis of a more detailed calorimetric and track analysis and the matching between tracks and hits in calorimeters and in scintillators. The level 2 trigger rate was between 10 and 15 Hz. The accepted events were then forwarded to the level 3 trigger.

The level 3 made its decision using fully digitized signals from all subdetectors. The accurate digital data with its higher resolution and granularity allowed tighter cuts and thresholds to be applied, compared to the lower level triggers. The final L3 event rate written on tape was about 3-6 Hz.

Energy Trigger

The energy trigger was one of the level 1 subtriggers and processed signals from the BGO calorimeter.[15] It was the only trigger that could accept single photon events and was of special importance to my analysis. As described in Section 4.2.3, the preamplifier output of each BGO crystal was available to the trigger. To reduce the number of channels in the readout, the signals from the barrel calorimeter were grouped into *blocks* of 30 crystals each. The barrel was divided into 32 azimuthal (ϕ) and 8 polar (θ) segments, resulting in a total of 256 blocks. In a similar manner,

---

[15] It also handled signals from the HCAL and the luminosity monitor. However, those were not relevant to the single-photon selection.

the BGO endcaps were also divided into segments giving an additional 256 channels. Analog signals from the 512 channels formed the input to the energy trigger. Each of these channels was digitized by a system of Fast Encoding and Readout ADC (FERA) modules. The FERA system used the charge collected by the readout photodiodes during a 2 μs gate, in contrast to the 11 μs gate of the BGO "complete" readout.

The energy trigger employed several algorithms to reject the background and noise events. The most notable among them were the following:

- **The total energy trigger.** The total energy measured in the BGO was required to be greater than about 30 GeV.
- **The BGO cluster trigger.** This algorithm performed a search for clusters in the BGO. For a positive decision, at least one cluster with energy above approximately 5 GeV had to be present.
- **The single photon trigger (barrel only).** This trigger was developed specifically to accept single-photon events in the BGO barrel. It required a single, isolated BGO cluster with an energy above about 80% of the total energy measured by the BGO [125]. The threshold of this trigger was set as low as possible, at approximately 0.9 GeV.

In summary, the L3 trigger acceptance for single-photon events was limited to the region of $E_\gamma \geq 0.9$ GeV (barrel) and $E_\gamma \geq 5$ GeV (endcaps), where E_γ is the photon energy. The performance of the energy trigger will be discussed in Chapter 6 (Section 6.3.2).

4.2.10 Detector Reconstruction and Simulation in L3

For each event accepted by the trigger system, an *event record* was written on tape. It consisted of "raw" digitized data from all L3 subdetectors. The off-line event reconstruction followed several steps. First, the raw data was read and decoded. Next, the reconstruction for signals from each subdetector was performed. For example, the energy deposited in each BGO crystal was calculated from the electronic pulse measured by the readout system. Finally, a common software package was used to group individual detector hits into meaningful objects, such as calorimetric clusters or tracks in TEC and muon chambers. The obtained information was stored on disk and was available to the L3 community for further analysis.

The Detector Simulation

In order to compare results from data with various theoretical predictions, the detector response to any particular process is calculated. The complexity of the detector makes it impossible to perform such calculations analytically. Instead, various Monte Carlo techniques are used to simulate the detector response [126].

Monte Carlo simulation of the L3 detector proceeds via two steps. The first step is to create *event lists* using a Monte Carlo generator corresponding to a theoretical description of any given interaction process. The event lists contain the four-momenta of the generated particles, their decay lengths and vertices of creation, the expected production cross section, and other information. Event generators used in L3 form a common library, and their output is standardized to simplify further analysis procedures. Different event generators are written using different coding techniques and, sometimes, even different programming languages. The conversion of a new generator as provided by its authors to the standard L3 format is usually the responsibility of an L3 physicist interested in using this generator in his or her analysis. Such conversion generally involves rewriting large parts of code and is not an easy task.

The second step of the simulation consists in propagating the generated particles through a detailed representation of the L3 detector, which simulates energy loss, scattering, and showering of particles in the detector materials. This program was written using the `GEANT3` detector description and simulation tool [127]. The same program is used to simulate the response of each active detector element to particles passing through it. Detector imperfections (such as dead or noisy channels in the calorimeters, disconnected TEC sectors, etc.) are also taken into account.

After the “full” detector simulation, the generated events are stored on disk and can be compared directly with the L3 data events.